RSC Advances

PAPER

View Article Online
View Journal | View Issue

Cite this: *RSC Adv.*, 2018, **8**, 27973

A mesoporous tungsten carbide nanostructure as a promising cathode catalyst decreases overpotential in Li–O_2 batteries†

Shuo Liu,‡[ab] Chengdong Wang, ‡[a] Shanmu Dong,[a] Hongbin Hou,[a] Ben Wang,[b] Xiaogang Wang,[a] Xiao Chen*[a] and Guanglei Cui *[a]

Lithium–oxygen (Li–O_2) batteries as promising energy storage devices possess high gravimetric energy density and low emission. However, poor reversibility of electrochemical reactions at the cathode significantly affects the electrochemical properties of nonaqueous Li–O_2 batteries, and low charge–discharge efficiency also results in short cycle-life. In this work, functional air cathodes containing mesoporous tungsten carbide nanoparticles for improving the reversibility of positive reactions in Li–O_2 cells are designed. Mesoporous tungsten carbides are synthesized with mesoporous carbon nitride as the reactive template and carbon source. And mesoporous tungsten carbides in cathode materials display better electrochemical performance in Li–O_2 cells in comparison with mesoporous carbon nitride and hard carbon. Tungsten carbide-1 (WC-1) with larger specific surface area promotes reversible formation and decomposition of Li_2O_2 at the cathode and lower charge overpotential (about 0.93 V) at 100 mA g^{-1}, which allows the Li–O_2 cell to run up to 100 cycles. In addition, synergistic interaction between WC-1 and LiI could further decrease the charging overpotentials of Li–O_2 cells and improve the charge–discharge performances of the Li–O_2 cells. These results indicate that mesoporous electrocatalysts can be utilized as promising functional materials for Li–O_2 cells to decrease overpotentials.

Received 11th July 2018
Accepted 31st July 2018

DOI: 10.1039/c8ra05905e

rsc.li/rsc-advances

Introduction

Lithium–oxygen (Li–O_2) batteries have attracted more and more attention due to their high energy density, which is higher than that of conventional rechargeable Li-ion batteries.[1,2] Nevertheless, Li–O_2 batteries are limited in practical applications due to several shortcomings such as low rate performance, limited cycle life, and poor reversibility. Based on the electrochemical process in Li–O_2 batteries, poor reversibility of the oxygen reduction reaction (ORR) and oxygen evolution reaction (OER) could induce the loss of battery capacity.[1] Hence, the design of functional cathodes with good ORR and OER activities is important for promoting cycling performances of Li–O_2 batteries. Several kinds of cathodes with ORR and OER catalysts such as noble metal,[3] carbon materials,[4,5] and transition-metal oxides/nitrides[6–11] have been focused on in the past. For example, porous carbon is a desired choice for cathodes due to the outstanding electronic conductivity, the tunable porous structures and the high specific surface area,[4,5] but the poor OER activity leads to high charging potentials over 4.5 V causing negative reactions to the electrolyte and electrode.[4,5]

The charge–discharge overpotential plays an important role in cycling performances of Li–O_2 batteries.[12–19] Many electrocatalysts such as mesoporous titanium nitride[20,21] are designed to decrease the overpotential. Noble metal catalyst Ru supported on three-dimensional reduced holey graphene oxide could reduce the overpotential of Li–O_2 to about 0.9 V at first cycle and maintain the <1 V overpotential until 19 cycles.[3] According the cost of noble metal, non-noble catalysts are developed.[4–11] Transition metal carbides have also received extensive interest as air cathode materials due to their good catalytic activities and stability during ORR and OER.[22–25] For example, the MoxC-based electrocatalysts display good performance to reduce overpotential in Li–O_2 batteries.[24,25] Similar to MoxC, tungsten carbide (WC) has excellent electrocatalytic performance in fuel cell,[26–30] which makes it an interesting potential as a cathode material in Li–O_2 batteries. And WC coating on cathode reduced the overpotential to 0.88 V.[31] However, there are fewer reports on the effect of catalysts surface area in Li–O_2 cathode on performance of batteries. Several tungsten carbides used in Li–O_2 batteries are relatively larger particles with a smaller specific surface area.[32–35] The effect of specific surface area of electrocatalysts on

---

[a] *Qingdao Industrial Energy Storage Research Institute, Qingdao Institute of Bioenergy and Bioprocess Technology, Chinese Academy of Sciences, No. 189 Songling Road, 266101 Qingdao, PR China. E-mail: chenxiao@qibebt.ac.cn; cuigl@qibebt.ac.cn*

[b] *College of Environment and Safety Engineering, Qingdao University of Science and Technology, Qingdao 266042, PR China*

† Electronic supplementary information (ESI) available: Structural characterization of SBA-15 and g-C_3N_4; cycles of Li–O_2 cells for different electrochemical catalysts. See DOI: 10.1039/c8ra05905e

‡ These authors contributed equally to this work.

electrochemical activities in fuel cells has been investigated in recent.[36–38] For example, Co-based catalysts dispersed on porous supports with large active area displays good performance for hydrogen evolution reaction (HER) and oxygen evolution reactions (OER).[36] According to previous reports, the high electrochemical active area may enhance the electrochemical catalytic activities of electrocatalysts.[6,7,9] Although the electrocatalysts used in Li–O_2 batteries in many reports have relative large surface area, the relationship between surface area of catalysts and performances of batteries has not been systematic investigated.[6–11]

In this study, tungsten carbide structures are prepared through calcining tungsten precursors with mesoporous carbon nitride (g-C_3N_4) in inert gas at certain temperature. The precursor compositions and reaction temperature could change the size and surface area of the final tungsten carbide structures. Herein, the effects of specific surface area of electrocatalysts on overpotential of Li–O_2 cells have been investigated. Mesoporous tungsten carbide structures (WC) are used in highly efficient air cathode of Li–O_2 cells to reduce overpotentials, which endow cells with good cycling performances. WC-1 could significantly reduce the overpotential of Li–O_2 cell, which is comparable to performances of state-of-the-art electrocatalysts used in Li–O_2 cells in recent reports (Table S1†). These results the electrocatalysts with large surface area could effectively reduce the overpotential of cells. It demonstrates the hierarchical electrocatalysts with large surface area could be designed to enhance cycling performances of Li–O_2 batteries.

Experimental

Synthetic procedures

Pluronic P123 ($EO_{20}PO_{70}EO_{20}$) as a template agent was used to prepare SAB-15 mesoporous materials.[39] The data of SBA-15 can be obtained in ESI file (Fig. S1).† And SBA-15 was acidified using hydrochloric acid at 80 °C for one day and dried at 80 °C for 12 hours. Then, acid-treated SBA-15 with cyanamide was heated at 60 °C under sonication and vacuuming for several hours. Third, the excess cyanamide was washed by water. The obtained solid was dried and calcined at high temperatures. The yellow powders were etched with NH_4HF_2 aqueous solution for one day to remove template. Then the mixture was filtrated, and the solid was washed with water and ethanol for three times.

For synthesis of WC, mesoporous carbon nitride (g-C_3N_4) template was added into ethanol solution of WCl_6 (99.9%) to allow the precursor enter the channel of g-C_3N_4 and the weight ratio between the precursor compounds and g-C_3N_4 was 1 : 1.[26] The final mixture was treated at 950 °C in an alumina crucible under N_2 at certain heating rate.[26]

Characterizations

X-ray diffractometer (XRD) was used to confirm crystal structure of catalysts at the power 9 kW (SmartLab). Scanning electron microscopy (SEM, Hitachi S-4800) and transmission electron microscope (TEM, TF30) were used to characterized morphologies and structures of the samples. X-ray photoelectron spectra (XPS) were collected with an ESCALAB 250Xi. Nitrogen adsorption–desorption data were obtained to investigate specific surface area and pore size distribution (Autosorb iQ2).

Li–O_2 cell assembly and electrochemical measurements

Nonaqueous Li–O_2 cells were assemblied. To prepare the air cathode electrodes, tungsten carbide (20 wt%) as catalyst was mixed with super-P (SP, 70 wt%) and polytetrafluoroethylene (PTFE, 10 wt%) binder. The Swagelok Li–O_2 batteries were assemblied in glove box filled with Ar, which contained lithium foil as the anode and a glass fibre membrane as separator. The electrolyte was 1 M bis(trifluoromethanesulfonyl) imide lithium (LiTFSI)/tetraethylene glycol dimethyl ether (TEGDME). The cell worked in pure oxygen to decrease negative effects from water and CO_2. All of the electrochemical measurements were tested using a LANHE battery testing system at 25 °C. All electrochemical data were calculated based on the weight of cathode materials with 0.5 mg cm^{-2}.

Results and discussion

The morphological and structural features of g-C_3N_4 are clearly revealed from SEM data in Fig. 1. As shown in Fig. 1a and b, the rodlike morphologies of g-C_3N_4-1 is similar with that of SBA-15 templates, even the ordered grooves on the surface. The precursor of g-C_3N_4 could penetrate into SBA-15 mesopores by vacuumizing and polymerize at elevated temperature, which makes it to reversely replicate the mesoporous structure of SBA-15.[40,41] Ordered textural framework of g-C_3N_4-1 is further evidenced by TEM image in Fig. 1c and the size of pore is about 5 nm. There are clear and orderly channel structures in g-C_3N_4-1 just reverse replica of SBA-15 (Fig. S1†), which may make the g-C_3N_4-1 serve as a good template and support.[42,43] And Nitrogen adsorption–desorption characterization is performed to investigate the porous properties of g-C_3N_4 and tungsten carbides. The specific surface area and pore volume of g-C_3N_4-1 with

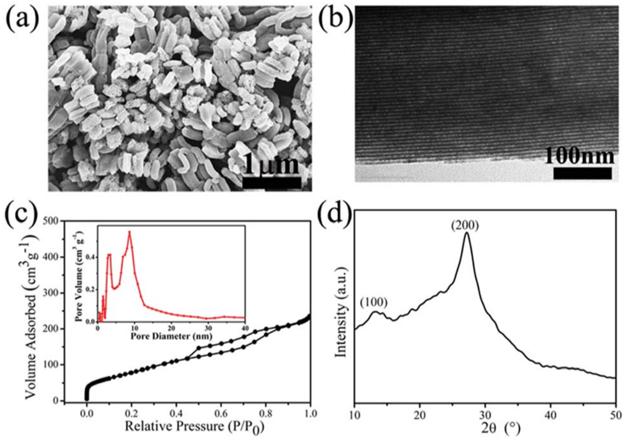

Fig. 1 Structural characterization of g-C_3N_4-1. (a) FE-SEM image of g-C_3N_4-1, (b) TEM image of g-C_3N_4-1, (c) nitrogen adsorption–desorption isotherms and pore size distribution of g-C_3N_4-1, (d) XRD patterns of g-C_3N_4-1.

highest specific area are 336.0 $m^2 g^{-1}$ and 0.36 $cm^3 g^{-1}$, which is used as template for preparation WC-1. The distribution of pore diameter in Fig. 1c is mainly located at 4 nm and 9 nm, which allows the precursor solution of WC penetrate into pores. In addition, nitrogen adsorption–desorption isotherms of others g-C_3N_4 with different specific surface area are displayed in Fig. S2.† The specific surface area of g-C_3N_4 become large with increase of vacuum time, which may originate from better filling of g-C_3N_4 precursor into channels of SBA-15. Fig. 1d shows the XRD patterns of g-C_3N_4-1. Two peaks can be confirmed at 27.4° for (200) planes and 13.0° for (100) planes, which are the characteristic peaks of graphitic-like C_3N_4.[39] In FT-IR spectra (Fig. S2†), the peak at 808 cm^{-1} is assigned to bending vibration of heptazine ring, the bands at 1250–1650 cm^{-1} are corresponding to stretching mode of heptazine ring and the band at 3100–3400 cm^{-1} is ascribed to the stretching vibration of N–H in residual NH_2.[43]

The structural features of WC samples are presented in Fig. 2a–e, showing different of nanostructures and specific surface areas. Four WC samples possessed different specific surface areas are synthesized by g-C_3N_4 with different specific surface areas (Table 1). WC-1 was synthesized by g-C_3N_4-1 with largest specific surface area. However, the WC nanoparticles did not fully replicate the mesoporous structure, which may be induced by high reaction temperature above 900 °C during synthesis of WC materials. The g-C_3N_4 could decompose above 700 °C,[44] which may cause the damage of mesoporous channel. In high-resolution TEM image (HR-TEM, Fig. 2e), crystal lattice of WC-1 particles is corresponding to the (010) plane of the tungsten carbide, which is in corresponding to the XRD spectrum (Fig. 2f).[26] As in previous studies, XRD patterns of WC nanoparticles could vary with the weight ratio between starting precursor and carbon source while keeping the temperature constant at 950 °C. In this study, usage of ethanol, heating rate, calcination temperature between 900 °C and 1000 °C are no significant effects on specific surface area and size of final WC in this study. In addition, the peaks at 40.26° reflect of the metal W in the WC-3 and WC-4, which illustrates a little tungsten form in tungsten carbide nanoparticles during calcination.[26] These results indicate that WC nanoparticles with different specific surface areas are practicable *via* g-C_3N_4 as carbon source and template.

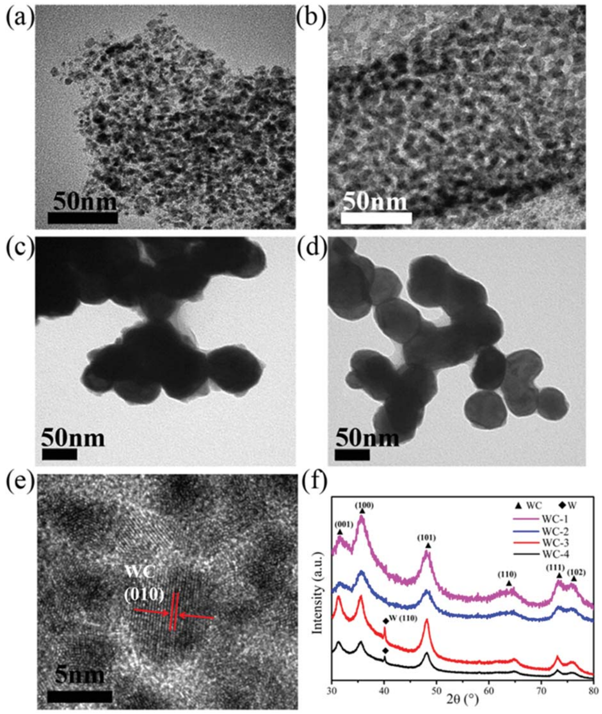

Fig. 2 The structural characterization of WC. TEM images of WC-1 (a), WC-2 (b), WC-3 (c), WC-4 (d); (e) HR-TEM images of WC-1; (f) XRD patterns of WC.

Table 1 Specific surface area of different samples

Sample name	Abbreviation	Specific surface area, $m^2 g^{-1}$
Graphitic C_3N_4-1	g-C_3N_4-1	336.0
Graphitic C_3N_4-2	g-C_3N_4-2	259.0
Graphitic C_3N_4-3	g-C_3N_4-3	223.0
Graphitic C_3N_4-4	g-C_3N_4-4	160.0
Tungsten carbide-1	WC-1	121.2
Tungsten carbide-2	WC-2	67.5
Tungsten carbide-3	WC-3	24.6
Tungsten carbide-4	WC-4	5.6

X-ray photoelectron spectroscopy (XPS) is applied to study the surface properties of samples. W4f and C1s spectra are recorded in Fig. 3a and b. In XPS spectra, two strong signals at 32.0 and 34.2 eV are corresponding to W4$f_{5/2}$ and W4$f_{7/2}$ of the WC-1 (Fig. 3b), which agrees with that of WC in previous report.[26] Fig. 3c presents nitrogen adsorption–desorption isotherms curves of mesoporous WC. BET surface areas are 121.2 $m^2 g^{-1}$, 67.5 $m^2 g^{-1}$, 24.6 $m^2 g^{-1}$ and 5.6 $m^2 g^{-1}$ for WC-1, WC-2, WC-3 and WC-4, respectively. And g-C_3N_4 with greater surface area as template could accommodate more precursor of WC nanoparticles to produce WC with larger specific surface area. The results demonstrate specific surface area of g-C_3N_4 could influence structure of WC.

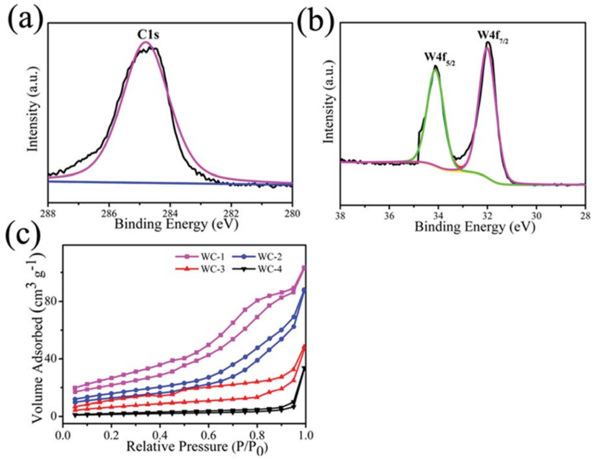

Fig. 3 (a and b) C1s and W4f spectra of WC-1, (c) nitrogen adsorption–desorption isotherms of mesoporous tungsten carbides.

We test electrocatalytic activity of different catalysts in 1 M LiTSFI/TEGDME to study electrocatalytic performances of mesoporous tungsten carbides in Li–O_2 cell. Fig. 4a gives the initial voltage curves of mesoporous tungsten carbides (WC), g-C_3N_4 and hard carbon (C). It is observed that the Li–O_2 cells with mesoporous tungsten carbides WC-1 and WC-2 show lower overpotential than those cells with WC-3 and WC-4, g-C_3N_4 and C electrodes throughout the first discharge. In addition, the Li–O_2 cell with WC-1 exhibits the lowest overpotential (0.93 V at first cycle) through reducing the charging voltage, which indicates WC-1 displayed good ORR activity. The property of reducing overpotential for WC-1 has been compared with state-of-the-art electrocatalysts in Table S1.† For the catalysts listed in Table S1,† the overpotentials of Li–O_2 cells at first cycle are lower than 1.30 V. And the catalysts containing Mo_2C could reduce the overpotential to less than 0.5 V.[11] The ability of reducing the overpotential of WC-1 is comparable to that of state-of-the-art electrocatalysts used in Li–O_2 cells in recent reports (Table S1†). The cycling stabilities of WC, g-C_3N_4 and C are also evaluated in Fig. 4b and d. The cycle profiles of WC-1 show relatively stable discharge voltage plateau around 2.7 V, and charge voltage plateau increases gradually from 3.6 V to 4.1 V when running at fixed capacity of 500 mA h g^{-1} during 100 cycles. The charge platform of Li–O_2 cells presents much more stable during cycling under low current density. It is indicated that Li–O_2 cell with WC-1 electrode gives favorable combination between initial capacity and cycle performance. Li–O_2 cells containing WC-3 and WC-4, g-C_3N_4 and C electrodes display lower electrochemical performances than those with WC-1 and WC-2 electrodes (Fig. S3†). In addition, the cell with WC-1 can display a discharge capacity of 665 mA h g^{-1} at current density of 500 mA g^{-1}, as shown in Fig. 4c. The stable cycles for Li–O_2 cell were reduced to 50 times at 1000 mA h g^{-1} (Fig. S4†), which should be attributed to side reactions caused by a large amount of lithium peroxide.[45] It's obviously that the Li–O_2 cells with WC-1 and WC-2 electrodes present superior cycling performance than those with WC-3 and WC-4 in Li–O_2 cells, which could be attributed to the better catalytic activity and larger surface area of WC-1 and WC-2.

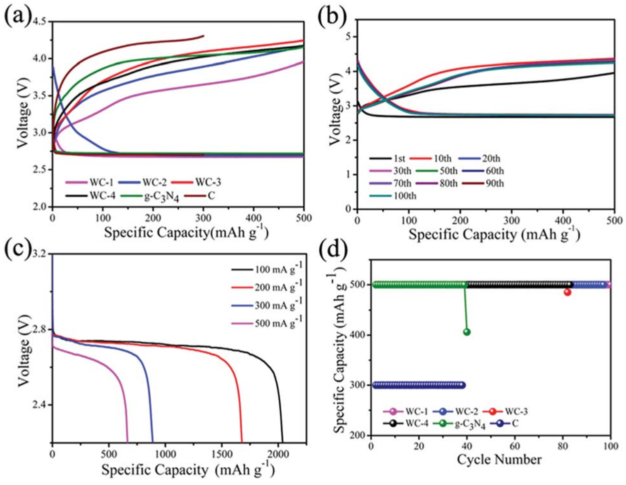

Fig. 4 (a) Full discharge–charge capacity profiles of Li–O_2 cells with WC-1, WC-2, WC-3, WC-4, g-C_3N_4 and C at current density 100 mA g^{-1}. (b) Cycles of Li–O_2 cells with WC-1 under fixed capacity of 500 mA h g^{-1} at current density 100 mA g^{-1}. (c) WC-1 cathodes at different current densities. (d) The cycling performances of the six cells with WC, g-C_3N_4, and C.

The structural properties of discharge products are important to the electrochemical behavior of Li–O_2 cells. It is known that Li_2O_2 as discharge product with small size often exhibits better electrochemical property with low overpotential.[46,47] In previous studies, charge voltage plateaus reduced as the decrease of Li_2O_2 size, which was attributed to the decrease of polarization and enhancement of oxidation reaction rate of Li_2O_2.[24,25] SEM images (Fig. 5b) of electrodes with WC-1 demonstrate that discharge products cover the electrode surface after first discharging process. The toroid-like Li_2O_2 is found in SEM image of cathode products (Fig. 5c) after first discharge process, which is corresponding to formation of Li_2O_2 in solution (Fig. 6).[48] XRD pattern of cathode electrode at the first discharged status exhibits two peaks at 32.8° and 34.9°, in accord with the (100) and (101) crystal planes of Li_2O_2 (Fig. 5d).[48] However, XRD patterns do not show characteristic peaks of Li_2O_2 for the pristine electrode, first charging electrode, and 100th charged electrode. These results indicate the Li_2O_2 could form in discharge stage and disappear after charging. These results proved that WC-1 with larger specific surface area could promote the reversible formation and decomposition of Li_2O_2 efficiently with greatly reducing overpotential and improve cycle property of Li–O_2 cells.

For optimal performance, lithium iodide (LiI) as a redox mediator (RM) is employed in the tungsten carbides-based Li–O_2 cells, which facilitates decomposition of Li_2O_2 and decreases charging overpotential by improving the transfer of charge in charging.[49] The lower overpotential in the cycles is beneficial for cycle performance of Li–O_2 cell at a constant capacity condition. Fig. 7a displays initial voltage profiles of Li–O_2 cells using tungsten carbides and LiI. Li–O_2 cells containing WC with LiI both show almost identical charging profiles. It is observed that the Li–O_2 cell with WC-1 shows lower overpotentials than those

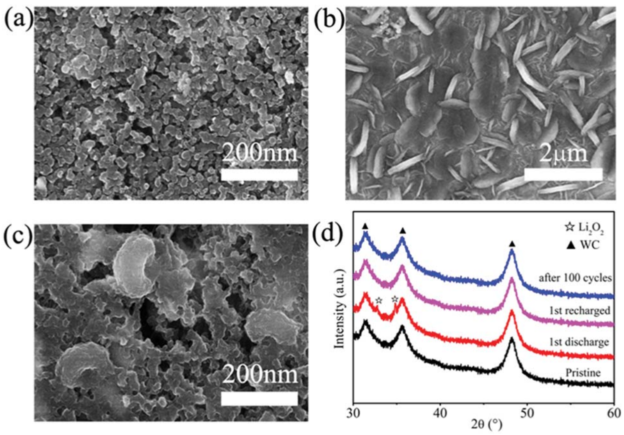

Fig. 5 SEM images of WC-1 cathode electrode at the pristine (a), after first discharge (b), and Li_2O_2 morphology in cathode electrode after first discharge (c). (d) XRD patterns of cathode electrode at different charge–discharge status.

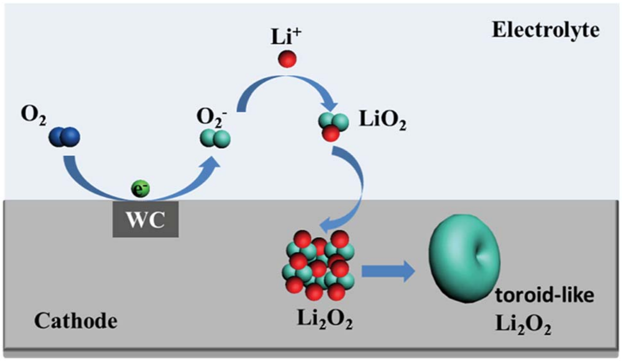

Fig. 6 Proposed formation mechanism of toroid-like Li_2O_2 in presence of WC.

with other tungsten carbides at the first cycle with LiI. In addition, the charging overpotentials with LiI decrease to 0.34 V for WC-1, while the charging overpotentials are 0.65 V, 0.82 V, 0.80 V for WC-2, WC-3 and WC-4, respectively. It is indicated that transfer of charge is more key than electronic transmission of cathode for outstanding charging process.

The cycle performances of mesoporous tungsten carbides are investigated under fixed capacity of 500 mA h g^{-1} (Fig. 7). Cycle profile of Li–O_2 cell with WC-1 electrode when fixing capacity at 500 mA h g^{-1} shows relatively stable discharge plateau around 2.7 V. In addition, the charging plateau of Li–O_2 cell with WC-1 electrode gradually increases from 3.1 V to 3.5 V during 97 cycles. The charge platform of Li–O_2 cell using WC-1 presents much more stable than that of other Li–O_2 cells. As contrast, Li–O_2 cell containing WC-2, possessing lower surface area than WC-1, shows relatively stable discharge–charge voltage platform even after 70 cycles. Due to WC only used as cathodic catalyst, decomposition of electrolyte also occurred inducing by reactive intermediate.[31] In addition, Li–O_2 cells with WC-1 and WC-2 also appear lower overpotential than those with WC-3 and WC-4. We suspect that the mesoporous tungsten carbides displayed excellent electrochemical properties in Li–O_2 cell are closely relative to the mesoporous structure. As transition metal carbides, mesoporous structure with large specific surface area may provide more catalytic sites and perform better electrochemical properties.

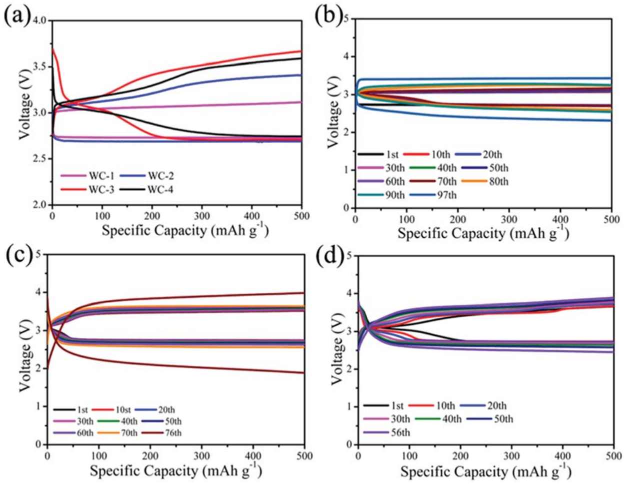

Fig. 7 Electrochemical performances of Li–O_2 cells with different cathode electrodes. Full discharge–charge capacity profiles of Li–O_2 cells with WC-1, WC-2, WC-3 and WC-4 at 100 mA g^{-1} (a). Charge–discharge curves of Li–O_2 cells under fixed capacity of 500 mA h g^{-1} at 100 mA g^{-1} and different cycles: (b) with WC-1 and LiI, (c) with WC-2 and LiI, (d) with WC-3 and LiI.

Conclusions

In summary, we successfully synthesized tungsten carbide nanoparticles from the confinement of the pores of the g-C_3N_4 nanostructure. Mesoporous WC with different specific surface areas shows different electrochemical properties in Li–O_2 cells. Mesoporous tungsten carbide with higher surface area could display a better discharge capacity 2035 mA h g^{-1} at 100 mA g^{-1} in non-aqueous Li–O_2 cell. Due to the mesoporous structure and good catalytic properties, WC with higher surface area could promote Li–O_2 cells to run over 90 cycles when capacity is fixed at 500 mA h g^{-1}. In addition, specific surface area of mesoporous WC is larger, charging overpotential of Li–O_2 cell is lower and with the assistance of LiI, the overpotentials of Li–O_2 cells could be further decreased for the WC electrocatalyst. In principle, transition metal carbides with mesopores may be used as outstanding electrocatalysts to enhance properties of Li–O_2 cells by enhancing reaction reversibility in cathode.

Conflicts of interest

There are no conflicts to declare.

Acknowledgements

This work was supported by the National Science Fund for Distinguished Young Scholars (51625204), Key Scientific and Technological Innovation Project of Shandong (Grant No. 2017CXZC0505), the Shandong Provincial Natural Science Foundation (No. ZR2014BQ004), and the National Natural Science Foundation of China (Grant No. 21473228). Liu thank Dr Zhonghua Zhang and Dr Jianjiang He for their suggestions to the manuscript. We also thank the support from Qingdao Key Lab of Solar Energy Utilization and Energy Storage technology.

References

1 G.-H. Lee, S. Lee, J.-C. Kim, D. W. Kim, Y. Kang and D.-W. Kim, *Adv. Energy Mater.*, 2017, **7**, 1601741.
2 J. Kang, J. Kim, S. Lee, S. Wi, C. Kim, S. Hyun, S. Nam, Y. Park and B. Park, *Adv. Energy Mater.*, 2017, **7**, 1700814.
3 S. D. Lacey, D. J. Kirsch, Y. Li, J. T. Morgenstern, B. C. Zarket, Y. Yao, J. Dai, L. Q. Garcia, B. Liu, T. Gao, S. Xu, S. R. Raghavan, J. W. Connell, Y. Lin and L. Hu, *Adv. Mater.*, 2018, **30**, 1705651.
4 F. Qiu, P. He, J. Jiang, X. Zhang, S. Tong and H. Zhou, *Chem. Commun.*, 2016, **52**, 2713–2716.
5 W.-H. Ryu, F. S. Gittleson, M. Schwab, T. Goh and A. D. Taylor, *Nano Lett.*, 2015, **15**, 434–441.

6 X.-Z. Zhang, D. Han, Y.-B. He, D.-Y. Zhai, D. Liu, H. Du, B. Li and F. Kang, *J. Mater. Chem. A*, 2016, **4**, 7727–7735.

7 K. R. Yoon, K. Shin, J. Park, S.-H. Cho, C. Kim, J.-W. Jung, J. Y. Cheong, H. R. Byon, H. M. Lee and I.-D. Kim, *ACS Nano*, 2018, **12**, 128–139.

8 S. A. Cho, Y. J. Jang, H.-D. Lim, J.-E. Lee, Y. H. Jang, T.-T. H. Nguyen, F. M. Mota, D. P. Fenning, K. Kang, Y. Shao-Horn and D. H. Kim, *Adv. Energy Mater.*, 2017, **7**, 1700391.

9 S. H. Kim, Y. J. Lee, D. H. Kim and Y. J. Lee, *ACS Appl. Mater. Interfaces*, 2018, **10**, 660–667.

10 J. Zhang, C. Zhang, W. Li, Q. Guo, H. Gao, Y. You, Y. Li, Z. Cui, K.-C. Jiang, H. Long, D. Zhang and S. Xin, *ACS Appl. Mater. Interfaces*, 2018, **10**, 5543–5550.

11 J. G. Kim, Y. Kim, Y. Noh, S. Lee, Y. Kim and W. B. Kim, *ACS Appl. Mater. Interfaces*, 2018, **10**, 5429–5439.

12 C. Cao, Y. Yan, H. Zhang, J. Xie, S. Zhang, B. Pan, G. Cao and X. Zhao, *ACS Appl. Mater. Interfaces*, 2016, **8**, 31653–31660.

13 B. M. Gallant, D. G. Kwabi, R. R. Mitchell, J. Zhou, C. V. Thompson and Y. Shao-Horn, *Energy Environ. Sci.*, 2013, **6**, 2518–2528.

14 J. Yi, S. Wu, S. Bai, Y. Liu, N. Li and H. Zhou, *J. Mater. Chem. A*, 2016, **4**, 2403–2407.

15 Z. Lyu, L. Yang, Y. Luan, X. R. Wang, L. Wang, Z. Hu, J. Lu, S. Xiao, F. Zhang, X. Wang, F. Huo, W. Huang, Z. Hu and W. Chen, *Nano Energy*, 2017, **36**, 68–75.

16 M. Asadi, B. Kumar, C. Liu, P. Phillips, P. Yasaei, A. Behranginia, P. Zapol, R. F. Klie, L. A. Curtiss and A. Salehi-Khojin, *ACS Nano*, 2016, **10**, 2167–2175.

17 M. He, P. Zhang, S. Xu and X. Yan, *ACS Appl. Mater. Interfaces*, 2016, **8**, 23713–23720.

18 S. Song, W. Xu, R. Cao, L. Luo, M. H. Engelhard, M. E. Bowden, B. Liu, L. Estevez, C.-M. Wang and J.-G. Zhang, *Nano Energy*, 2017, **33**, 195–204.

19 C. Shu, Y. Lin and D. Su, *J. Mater. Chem. A*, 2016, **4**, 2128–2136.

20 Y. Chang, S. Dong, Y. Ju, D. Xiao, X. Zhou, L. Zhang, X. Chen, C. Shang, L. Gu, Z. Peng and G. Cui, *Adv. Sci.*, 2015, **2**, 1500092.

21 B. G. Kim, C. Jo, J. Shin, Y. Mun, J. Lee and J. W. Choi, *ACS Nano*, 2017, **11**, 1736–1746.

22 X.-Z. Zhang, D. Han, Y.-B. He, D.-Y. Zhai, D. Liu, H. Du, B. Li and F. Kang, *J. Mater. Chem. A*, 2016, **4**, 7727–7735.

23 Y. Zhong, X. Xia, F. Shi, J. Zhan, J. Tu and H. J. Fan, *Adv. Sci.*, 2016, **3**, 1500286.

24 Y. Xing, Y. Yang, R. Chen, M. Luo, N. Chen, Y. Ye, J. Qian, L. Li, F. Wu and S. Guo, *Small*, 2018, 1704366.

25 G. Sun, Q. Zhao, T. Wu, W. Lu, M. Bao, L. Sun, H. Xie and J. Liu, *ACS Appl. Mater. Interfaces*, 2018, **10**, 6327–6335.

26 A. T. Garcia-Esparza, D. Cha, Y. Ou, J. Kubota, K. Domen and K. Takanabe, *ChemSusChem*, 2013, **6**, 168–181.

27 Z.-Y. Chen, C.-A. Ma, Y.-Q. Chu, J.-M. Jin, X. Lin, C. Hardacre and W.-F. Lin, *Chem. Commun.*, 2013, **49**, 11677–11679.

28 Y. Liu and W. E. Mustain, *ACS Catal.*, 2011, **1**, 212–220.

29 S. Zhang, Z. Huang, Z. Wen, L. Zhang, J. Jin, R. Shahbazian-Yassar and J. Yang, *Nano Lett.*, 2017, **17**, 3518–3526.

30 J. B. Varley, V. Viswanathan, J. K. Norskov and A. C. Luntz, *Energy Environ. Sci.*, 2014, **7**, 720–727.

31 B. S. Koo, J. K. Lee and W. Y. Yoon, *Jpn. J. Appl. Phys.*, 2015, **54**, 047101.

32 M. S. Bazarjani, M. M. Mueller, H.-J. Kleebe, C. Fasel, R. Riedel and A. Gurlo, *J. Mater. Chem. A*, 2014, **2**, 10454–10464.

33 Y. Yan, B. Xia, X. Qi, H. Wang, R. Xu, J.-Y. Wang, H. Zhang and X. Wang, *Chem. Commun.*, 2013, **49**, 4884–4886.

34 W. Cui, Z. Wu, C. Liu, M. Wu, T. Ma, S. Wang, S.-T. Lee and B. Sun, *J. Mater. Chem. A*, 2014, **2**, 3734–3740.

35 B. Liu, P. Yan, W. Xu, J. Zheng, Y. He, L. Luo, M. E. Bowden, C. M. Wang and J.-G. Zhang, *Nano Lett.*, 2016, **16**, 4932–4939.

36 Y. Yang, H. Fei, G. Ruan and J. M. Tour, *Adv. Mater.*, 2015, **27**, 3175–3180.

37 S. Han, Y. Feng, F. Zhang, C. Yang, Z. Yao, W. Zhao, F. Qiu, L. Yang, Y. Yao, X. Zhuang and X. Feng, *Adv. Funct. Mater.*, 2015, **25**, 3899–3906.

38 A.-R. Ko, Y.-W. Lee, J.-S. Moon, S.-B. Han, G. Cao and K.-W. Park, *Appl. Catal., A*, 2014, **477**, 102–108.

39 C. Z. Yu, J. Fan, B. Z. Tian, D. Y. Zhao and G. D. Stucky, *Adv. Mater.*, 2002, **14**, 1742–1745.

40 J. Zhang, F. Guo and X. Wang, *Adv. Funct. Mater.*, 2013, **23**, 3008–3014.

41 M. Tahir, C. Cao, N. Mahmood, F. K. Butt, A. Mahmood, F. Idrees, S. Hussain, M. Tanveer, Z. Ali and I. Aslam, *ACS Appl. Mater. Interfaces*, 2014, **6**, 1258–1265.

42 Y. Hou, J. Li, Z. Wen, S. Cui, C. Yuan and J. Chen, *Nano Energy*, 2014, **8**, 157–164.

43 H. Yu, L. Shang, T. Bian, R. Shi, G. I. N. Waterhouse, Y. Zhao, C. Zhou, L.-Z. Wu, C.-H. Tung and T. Zhang, *Adv. Mater.*, 2016, **28**, 5080–5086.

44 W.-J. Ong, L.-L. Tan, Y. H. Ng, S.-T. Yong and S.-P. Chai, *Chem. Rev.*, 2016, **116**, 7159–7329.

45 P. Zhang, Y. Zhao and X. Zhang, *Chem. Soc. Rev.*, 2018, **47**, 2921–3004.

46 J. Xie, Q. Dong, I. Madden, X. Yao, Q. Cheng, P. Dornath, W. Fan and D. Wang, *Nano Lett.*, 2015, **15**, 8371–8376.

47 J.-J. Xu, Z.-W. Chang, Y. Wang, D.-P. Liu, Y. Zhang and X.-B. Zhang, *Adv. Mater.*, 2016, **28**, 9620–9628.

48 K. Liu, H. Sun, S. Dong, C. Lu, Y. Li, J. Cheng, J. Zhang, X. Wang, X. Chen and G. Cui, *Adv. Mater. Interfaces*, 2017, **4**, 1700693.

49 Y. Li, S. Dong, B. Chen, C. Lu, K. Liu, Z. Zhang, H. Du, X. Wang, X. Chen, X. Zhou and G. Cui, *J. Phys. Chem. Lett.*, 2017, **8**, 4218–4225.